Towards a Practical Convex Formulation of Contact with Friction
PLEASE DO NOT DISTRIBUTE

Alejandro M. Castro

December 8, 2020

1 Introduction

Anitescu's convex relaxation of contact [1] has been in existence for 14 years. However to my knowledge there are no simulation/trajectory optimization codes out there that can exploit this formulation. In other words, the formulation is theoretically beautiful, but there are no practical solvers out there for it. The best reported solver for this formulation, later on presented by Anitescu in [2, 3], consists of a Projected Gauss-Seidel (PGS) iteration which is very well known not to converge in practice and it is usually stoped at a fixed number of iterations with an unknown amount of numerical error. Therefore, it is unclear even today whether Anitescu's formulation presents any advantage over other non-convex solution strategies. In [4] Todorov mentions a so called *generalized* projected Gauss-Seidel (though the details were never published), which generalizes PGS to deal with the true quadratic friction cone, anisotropy, torsional and rolling friction.

The objectives of this reasearch are:

1. To develop a *practical* solution strategy that is robust and has good scalability to number of bodies and contacts.

2. To extend the formulation to enable the simulation of soft deformable bodies with contact.

3. To properly quantify the *unphysical artifacts* introduced by the convex relaxation of the original physics.

4. To answer the questions "does the Convex formulation provide any significant advantage over other methods?", "are the unphysical artifacts introduced worth the price?"

5. To provide an open source implementation of this research that outperforms existing methods.

2 Formulation

The momentum equations for the dynamics of contact with friction read

$$\mathbf{M}\mathbf{v} = \mathbf{M}\mathbf{v}^* + \mathbf{J}^T\boldsymbol{\gamma} \tag{1}$$

where $\mathbf{v}^*$ are the generalized velocities of the system in the absence of contact forces and $\boldsymbol{\gamma}$ are the impulses in the contact space. For rigid body dynamics the formulation is completed with the following constraints

1. non-penetration constraint,

2. friction cone constraint and,

3. principle of maximum dissipation,

Anitescu introduces a *convex relaxation* of the contact problem in [1]. This relaxation is introduced as a modification to the complementarity constraint between penetration depth ϕ and normal impulse π as

$$0 < \phi - h\|\boldsymbol{v}_t\| \perp \pi > 0 \tag{2}$$

where h is the discrete time step.

This relaxation leads to a convex quadratic program with conic constraints as

$$\min_{\gamma \in \mathcal{F}} \ell(\boldsymbol{\gamma}) = \frac{1}{2}\boldsymbol{\gamma}^T \mathbf{W} \boldsymbol{\gamma} + \boldsymbol{r}^T \boldsymbol{\gamma} \tag{3}$$

where $\boldsymbol{\gamma}$ are the contact point impulses (i.e. with units of N · s), $\mathbf{W} = \mathbf{J}^T \mathbf{M}^{-1} \mathbf{J}$ is the Delassus operator (the inverse of the inertia matrix projected on the contact space), $\mathcal{F}$ is the feasible set of all contact impulses satisfying the cone constraint and, $\boldsymbol{r} = \boldsymbol{v}^* - \boldsymbol{v}_s$, with $\boldsymbol{v}_s$ a *stabilization velocity*. See [2, 3] for details.

3 Regularization

In [5, 4] Todorov introduces regulariztion to the formulation in 3, though the derivation is inspired on the Gauss's principle of least constraint. The regularized formulation reads

$$\min_{\gamma \in \mathcal{F}} \ell(\boldsymbol{\gamma}) = \frac{1}{2}\boldsymbol{\gamma}^T (\mathbf{W} + \mathbf{R})\boldsymbol{\gamma} + \boldsymbol{r}^T \boldsymbol{\gamma} \tag{4}$$

where $\mathbf{R}$ is a diagonal positive definite matrix that has the effect of making $\mathbf{W} + \mathbf{R} \succ 0$ since in general we only have $\mathbf{W} \succeq 0$.

4 Analytical Inverse Dynamics

Todorov shows that the regularized problem stated in Eq. (4) can be solved analytically if we know the next step velocity $\mathbf{v}$ that is, the *inverse dynamics* problem.

Following the work in [4], the force at each contact point can be solved, independently from all other contacts, from the following convex optimization problem

$$\min_{\gamma_i \in \mathcal{F}_i} \frac{1}{2}(\boldsymbol{\gamma}_i - \boldsymbol{y}_i)^T \mathbf{R}_i (\boldsymbol{\gamma}_i - \boldsymbol{y}_i) \tag{5}$$

with

$$\boldsymbol{y}_i = -\mathbf{R}_i^{-1}(\boldsymbol{v}_{c,i} + \boldsymbol{b}_i) \tag{6}$$

Todorov solves this problem for a more general case that considers anisotropic friction as well as rolling and torsional friction, leading to a small optimization problem in five dimensions. When only isotropic friction is considered, the problem can be solved in three dimensions and the solution looks significantly simpler. Here we present these analytical solutions as needed while details can be found in Appendix A.

Simpler expressions can be written if we consider the tangential and normal components separately. For each i-th contact we write the regularizing diagonal matrix as $\mathbf{R}_i = \text{diag}(\{R_{t,i}, R_{t,i}, R_{n,i}\})$. From now on, unless otherwise stated, we drop subindex i.

In the stiction region the analytical solution simple reduces to

$$\begin{aligned} \gamma_n &= -\frac{1}{R_n}(v_n + \phi_0/dt) \\ \boldsymbol{\gamma}_t &= -\frac{1}{R_t}\boldsymbol{v}_t \end{aligned} \tag{7}$$

that is, in the stiction region the contact forces behave as if they modeled strong viscous damping.

When there is sliding, region II in Fig. 9, Eq. (25) can be expanded into normal and tangential components as

$$\begin{aligned} \gamma_n &= \frac{1}{1 + \tilde{\mu}^2}\left(y_n + \mu\frac{R_t}{R_n}y_r\right) \\ \boldsymbol{\gamma}_t &= \mu\gamma_n\hat{\boldsymbol{t}} \end{aligned} \tag{8}$$

2

where $\tilde{\mu} = \mu(R_t/R_n)^{1/2}$ and the tangent vector is defined as $\hat{\boldsymbol{t}} = \boldsymbol{y}_t/\|\boldsymbol{y}_t\| = -\boldsymbol{v}_t/\|\boldsymbol{v}_t\|$.

Using the expressions for y_n and y_r in terms of velocities

$$
\begin{aligned}
y_n &= -\frac{1}{R_n}(v_n + b) \\
y_r &= \|\boldsymbol{y}_t\| = \frac{1}{R_t}\|\boldsymbol{v}_t\|
\end{aligned}
\tag{9}
$$

we can write the contact force as a function of the contact velocity as

$$
\begin{aligned}
\gamma_n &= \frac{1}{R_n(1 + \tilde{\mu}^2)}\left[-(v_n + b) + \mu\|\boldsymbol{v}_t\|\right] \\
\boldsymbol{\gamma}_t &= \mu\gamma_n\hat{\boldsymbol{t}}
\end{aligned}
\tag{10}
$$

4.1 Physical intuition and Maximum Dissipation Principle

Equation (10) provides a huge amount of intuition on the functional form of these forces.

Regarding the normal forces, lets ignore the term $\mu\|\boldsymbol{v}_t\|$ for a moment and lets take the limit $R_t/R_n \to 0$ (which implies $\tilde{\mu} \to 0$). In addition, lets take the normal regularization term as $R_n = (dt^2\,k)^{-1}$. In this case Eq. (10) for the normal impulse reduces to

$$
\gamma_n = -dt\,k\,(dtv_n + \phi_0) = -dt\,k\,\phi
\tag{11}
$$

That is, the normal impulse produced by the convex relaxation formulation amounts to the effect of a linear compliant force with spring constant k. The effect of $\tilde{\mu}$ is to change the effective value of this compliance. The term $\mu\|\boldsymbol{v}_t\|$ is very interesting. It is responsible for making the formulation convex, and responsible of unphysical artifacts in the contact forces (during sliding only) due to this new dependency of the normal force on the sliding velocity. This effect is analyzed with detail in Section 6 in a number of validation examples.

There is nothing in this formulation that enforces the well accepted principle of maximum dissipation. To my knowledge, it is not understood in the community what the effect of the convex formulation is on the maximum dissipation principle or if satisfied at all. Equation (10) helps answering this question. As shown by this equation, the friction force opposes the direction of the slip velocity and has magnitude $\mu\gamma_n$, the same results that would be enforced by the maximum dissipation principle. Notice that this result is independent of the ratio R_t/R_n and even if there is compliance in the normal direction, the result still holds in the limit to *Coulomb friction* when $R_t/R_n \to 0$.

5 Regularization Parameters

Todorov in [4] sets the regularization parameters as $R_i = \varepsilon N_{ii}$, where ε is a small dimensionless coefficient that controls the amount of regularization. Higher regularization will make the problem better conditioned though at the expense of large compliance and a poor stiction approximation. Lower regularization will converge to the *hard constraints* limit, however leading to a poorly conditioned formulation.

In this work we choose ε from an analysis of the time scales introduced by this regularization. The basic idea is that if the time scales introduced by this numerical compliance cannot be resolved by a given time step size dt, the system is effectively rigid. It essentially makes no difference on the results if regularization is decreased beyond this point.

For each contact point we define $g_i = \|\mathbf{W}_{ii}\|/3$ where $\mathbf{W}_{ii}$ is the 3×3 diagonal block of the Delassus operator $\mathbf{W}$. The factor 3 in our definition is so that g_i is the RMS value of the entries of $\mathbf{W}_{ii}$. This definition ensures that $g_i > 0$. g_i has unit of kg^{-1} and represents the inverse of an effective mass $m_i = g_i^{-1}$ for the i-th contact. For instance, for the contact between a point mass m and the ground we have $g_i = (3m)^{-1}$ and $m_i = 3m$, see Section 6.1.

Regularization in the normal direction introduces a numerical compliance of stiffness k, see Section 4.1, and this will therefore induce a dynamics with a natural frequency in the order of $\omega_n^2 = k/m_i$. This relates to the period T_n of this dynamics by $\omega_n = 2\pi/T_n$.

Since the time stepping scheme will not resolve time scales in the order or below the time step dt, we want to choose our regularization parameters so that the numerical dynamics introduced

cannot be resolved. We then make $T_n = \alpha dt$, with alpha $\alpha \approx 1.0$. Therefore we need for the stiffness $k = 4\pi^2 m_i/(\alpha^2 dt^2)$. We learned in Section 4.1 that $R_n = (dt^2 k)^{-1}$ and therefore we arrive to the final expression for our regularization in the normal direction

$$R_n = \frac{\alpha^2}{4\pi^2} g_i = \frac{\alpha^2}{4\pi^2} \|\mathbf{W}_{ii}\| \tag{12}$$

This is the same as Todorov's regularization taking $\varepsilon = \alpha^2/(4\pi^2) \approx 0.025\,\alpha^2$. This analysis shows us that:

- We can use a single parameter ε, independent of the time step, that leads to essentially the same numerically introduced artificial dynamics.

- When $\alpha = 1.0$ we have $\varepsilon = 0.025$ which introduces a fair amount of regularization into the system. However the numerical time scales are only within dt and are underresolved, as desired.

It is useful to estimate the amount of penetration for a point mass resting on the ground. In this case we have

$$
\begin{aligned}
\phi &= \frac{m\,g}{k} \\
&= \frac{\alpha^2}{4\pi^2} \frac{m}{m_i}\, g\, dt^2 \\
&= \frac{\alpha^2}{12\pi^2}\, g\, dt^2
\end{aligned} \tag{13}
$$

Taking $\alpha = 1.0$ and on Earth's gravity, a typical simulation time step of $dt = 10^{-3}$ s leads to $\phi \approx 8.3\times10^{-8}$ m and using a vary large simulation time tep of $dt = 10^{-2}$ s leads to $\phi \approx 8.3\times10^{-6}$ m, well within acceptable bounds for typical robotics applications.

There is another reason to choose $\alpha \approx 1.0$. As we will see in the example of Section 6.1, the numerical dynamics is close to being critically damped and numerical oscillations due to regularization are damped out within a few time steps, independent of step size (see Fig. 2). This is an expected result if we consider the stability analysis on an implicit Euler scheme, which reseembles this formulation very closely when we think of it as an implicit scheme on a multibody system with the compliant forces in Section 4. This is a very desired effect for us being interested on robotics applications with perfectly inelastic contact.

6 Test Cases

For these cases, unless otherwise specified, we use a regularization given by $\alpha = 1.0$.

6.1 Conveyor Belt

In this case a box of mass $m = 1$ kg that is only allowed to move in the vertical direction is placed on top of a conveyor belt moving horizontally in the $-x$ direction with a specified velocity $u_0 = -0.1$ m/s. The coefficient of friction is $\mu = 0.5$.

Given the regularization used in this formulation, a given amount of compliance given by R_n is expected and therefore the box will initially undergo a vertical motion until the *compliant* normal force balances the weight of the box. We will see however that due to the convex regularization the vertical motion is not only given by the normal compliance but also by the sliding velocity at contact.

We run this simulation using time steps in a geometric sequence with a common ration $\sqrt{10}$. Starting with the smallest value of $dt = 10^{-4}$ s to the larger value of $dt = 10^{-2}$ s.

6.1.1 Steady state solution

In the steady state the normal impulse γ_n will balance the weight of box $P = m\,g$, i.e. $\gamma_n = dt\,m\,g$. Also the normal velocity will be zero and therefore we can find out the steady state value of the

signed distance ϕ, or similarly the value of the stabilization velocity $b = \phi/dt$, from the analytical inverse dynamics Eq. 10 as

$$b = \frac{\phi}{dt} = \mu \|\boldsymbol{v}_t\| - (1 + \tilde{\mu}^2) R_n \gamma_n \tag{14}$$

For this problem we have that $\mathbf{J}_c = [0, 0, 1]^T$ and $\mathbf{M} = m$ and thus the Delassus operator is

$$\mathbf{W} = \begin{bmatrix} 0 & 0 & 0 \\ 0 & 0 & 0 \\ 0 & 0 & 1/m \end{bmatrix} \tag{15}$$

and therefore $g_i = (3m)^{-1}$.

Using the fact that $R_n = \varepsilon_n \, g_i = \frac{\alpha^2}{4\pi^2} g_i$, and that $\gamma_n = dt \, m \, g$ we can write the final expression for b as

$$b = \frac{\phi}{dt} = \mu \|\boldsymbol{v}_t\| - (1 + \tilde{\mu}^2) \frac{\alpha^2}{12\pi^2} g \, dt \tag{16}$$

In our regularization, α controls the amount of *compliance*. In the limit $\alpha \to 0$ we approach the rigid limit. Equation 16 shows us that in this limit the signed distance approaches the *positive* value $\phi = dt\mu\|\boldsymbol{v}_t\|$. This is consistent with previous work using Anitescu's formulation which does not introduce regularization, see [1, 6].

6.1.2   Initial conditions

If we replace values for $\alpha = 1.0$, $g = 10$ m/s^2 and a range of time steps, we find out that the effect of normal compliance is much smaller than the rigid limit value $\phi = dt\mu\|\boldsymbol{v}_t\|$ and thus ϕ in this problem is positive for relevant parameter values. This means that if we use an initial condition of $\phi = 0$ (rigid contact), the formulation will generate a very large impulse in order to violently push the box away from the moving belt. Therefore we prefer to initialize the vertical position of the box such that $\phi = dt\mu|u_0|$ to avoid this impulsive behavior.

6.1.3   Simulation results

Starting with the box at $z = dt\mu|u_0|$ and $\dot{z} = 0$ we simulate forward the dynamics of the box for 0.15 seconds, long enough to reach a steady state at which the normal compliance result from regularization balances the weight of the box.

Figure 1 plots the value of $b = \phi/dt$ for a range of time steps and two different values of σ_t ($R_t = \sigma_t R_n$). As predicted by Eq. (16), in the limit $dt \to 0$ we have that $b = \phi/dt = \mu\|\boldsymbol{v}_t\| = 0.05$ m/s. As the time step increases, the effect of the numerical compliance introduced for regularization becomes more evident and this value drops as the box sinks deeper into the moving belt. The value of R_t has a weaker though noticeable effect given the term $(1 + \tilde{\mu}^2)$ in Eq. (16).

The dynamics of the initial transient is shown in Fig. 2, which plots velocity a s function of time. It is interesting to note that when both time and velocity are normalized by the step size, solution results using different step sizes collapse into a single curve. From Fig. 2 we see that the initial transient lasts for about four time steps, regardless of the step size. We also observe that the normal velocity values are larger for larger time steps. This is consistent with the results in Fig. 1 since larger time steps lead to larger compliance and larger values of ϕ.

6.1.4   Verification with inverse dynamics

Equation (10) provides a way to verify the results obained from solving the forward problem. Once impulses $\boldsymbol{\gamma}$ are computed, we can update the contact velocities and in turn use these in Eq. (10) to obtain analytical inverse dynamics impulses $\boldsymbol{\gamma}_{ID}$. The relative difference $\|\boldsymbol{\gamma} - \boldsymbol{\gamma}_{ID}\|/\|\boldsymbol{\gamma}_{ID}\|$ provides an effective means to measure the error in the solution.

For this case we use the SCS solver in Drake with default tolerance of 10^{-5}. Figure 3 shows the computed relative errors as a function of time when using different time steps. There does not seem to be a specific trend on the errors as a function of time step, though the all fall below the default SCS tolerance of 10^{-5}.

We also tried the Gurobi solver. Even though the solution is accurately close to the expected values, comparison with inverse dynamics leads to meaningless results. The reason is that Gurobi
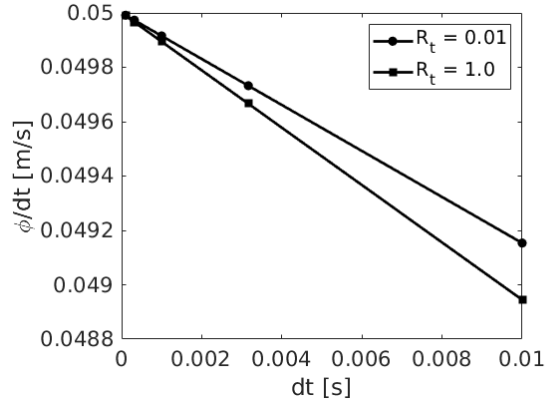
Figure 1: Steady state value of the *stabilization velocity* $b = \phi/dt$ as a function of the time step dt. As the time step approaches zero the scheme approximates to the *rigid* solution at which $\phi/dt \to \mu\|\boldsymbol{v}_t\|$. The slope of this line is consistent with the analytical solution in Eq. (16) due to the numerical compliance introduced by the regularization terms. The slope increases with larger values of R_t as predicted by Eq. (16).
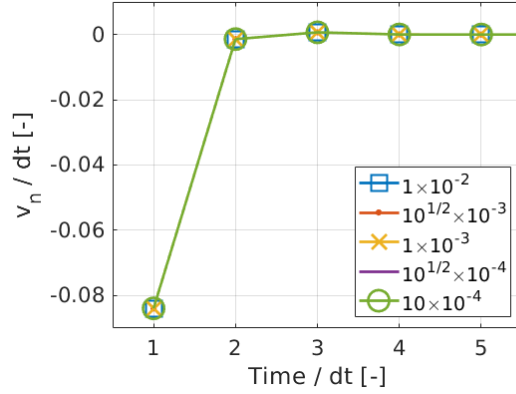

Figure 2: Normal velocity as a function of time. Simulation results using different time steps collapse into a single curve when both velocity and time are normalized using the time step.

being an interior point solver, introduces small errors in the computed impulses that places them strictly inside the friction cone. Unfortunately these small errors in the impulses, when propagated to the velocities, get severely amplified when these velocities are placed in Eq. (10). More concretely, small errors in velocity make $\boldsymbol{y}$ fall within the polar cone and therefore the resulting projection is zero.

This does not mean that the solution obtained by Gurobi is not accurate, but rather that the inverse dynamics solution is very sensitive to small changes in the contact velocities. This problem goes away when we are in the stiction region.

6.2 Sliding box

In this case a box of mass $m = 1$ kg with given an initial horizontal velocity $v = [1.0, 0.0, 0.0]$ m/s slides on the ground with friction coefficient $\mu = 0.5$ until it stops. The case is run with two time steps, $dt = 10^{-2}$ s and $dt = 10^{-3}$ s.

6.2.1 Inconsistent initial conditions

The naive initial condition for this case is to set the box to be in imminent contact with the ground, i.e. $z = 0$. We would think that the box would slightly sink into the ground due to the numerical compliance introduced by regularization, as we learned from Section 6.1. However we quickly find out from the Fig. (4) that this is not the case. Nevertheless we do find that this is a consistent
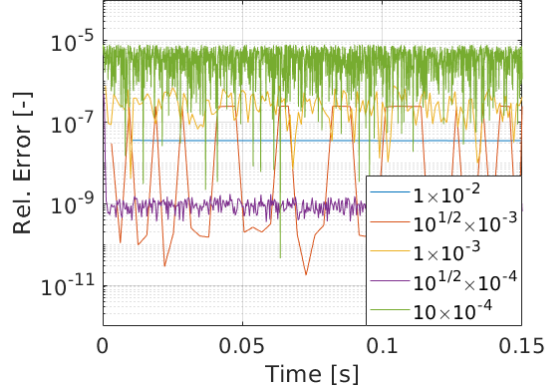
6

Figure 3: Relative error in the computed solution against the analytical inverse dynamics impulses from Eq. (10)

.

results previously reported in [6]. However the cause of this apparent artifact of the formulation is not investigated further in [6].

The answer to why we obtain this solution becomes evident when looking at the forces in Fig. (4). We find out that there is an initial large impulse at the very first time step and forces go to zero immediately after. The reason, is that this very large impulse pushed the box upwards into a short free flight trajectory. This explains the vertical velocity profile in Fig. (4) with the vertical velocity decreasing only due to the acceleration of gravity. The question now is, why is it that in the very first time step we obtain this very large impulse? the situation doesn't seem to improve when reducing the time step. The answer lies in the previous case in Section 6.1. We learned that when a contact is sliding, the contact distance will be slightly positive and approximately given by $z \approx dt\mu\|\boldsymbol{v}_t\|$. Therefore, when we initialize the problem with $z = 0$, this effectively sets the problem with a constraint violation given by $z \approx dt\mu\|\boldsymbol{v}_t\|$ and the solver must violently push the box out of this configuration. This initial transient is so violent that sets the box on free flight for almost 0.1 seconds.

6.2.2   Consistent initial conditions

The solution is then to initialize the box with $z = dt\mu\|\boldsymbol{v}_t\|$. The reader might argue that in general this is not possible. However, keep in mind that this kind of problems is impulsive and not quite physical. The reason is that in this problem the box is already in motion at $t = 0$ while in the real world we'd need to accelerate the box to that velocity in a finite time, giving the formulation enough time to settle to a proper value of z consistent with the contact constraints. For the sake of understanding this effect however, we set now the initial height of the box to $z = dt\mu\|\boldsymbol{v}_t\|$.

The new solution is shown in Fig. (5). Even though there is a small transient at the beginning of the simulation due to the numerical compliance introduced by the regularization, the solution is significantly smoother and better approximates the real problem we want to solve; the normal force $f_n = 10$ N quickly settles to balance the weight, the horizontal forces settles to the sliding force $f_t = -\mu\,f_n = 5$ N and the horizontal velocity decelerates at constant rate to a full stop.

6.2.3   Convex relaxation artifacts

We essentially observe three different artifacts in Fig. (5). The first one is the initial transient lasting about 4 time steps. This is related to the numerical compliance introduced by the regularization. As we learned from Fig. (1) compliance leads to a signed distance value that is slightly smaller than $dt\mu\|\boldsymbol{v}_t\|$.

The second artifact is the small negative vertical velocity as the box is sliding. This requires more analysis but we can explain it. As we learned, the box will glide at a distance from the ground approximately equal to $z \approx dt\mu\|\boldsymbol{v}_t\|$. However the box is decelerating at a constant rate due to the Coulomb friction force, i.e. $\dot{v}_t \approx -\mu g$. Therefore we can estimate the normal velocity as $v_n = \dot{z} \approx dt\mu\dot{v}_t = dt\mu^2 g$. This leads to the estimation $v_n \approx 2.5 \times 10^{-2}$ m/s when $dt = 10^{-2}$ s

and $v_n \approx 2.5 \times 10^{-3}$ m/s when $dt = 10^{-3}$ s, which is in perfect agreement with the results shown in Fig. (5).

The final and third artifact is the small peak in the normal force, which is not present in the true physical solution. Interestingly, this peak seems to have a magnitude independent of the time step. A deeper analysis will also explain this. When the box finally transitions to stiction, velocity drops to zero, as we see in the figure. As we already saw, there is a non-zero normal velocity v_n as the box slides and this velocity goes to zero when the box enters into stiction. Therefore there is a finite velocity change of magnitude v_n, an impact, that leads to an impulse $\Delta\gamma_n \approx m\,v_n \approx dt\mu^2 m\,g$. The change in the normal force is then $\Delta f_n = \Delta\gamma_n/dt \approx \mu^2 m\,g \approx 2.5$ N, independent of the time step. The peak in Fig. (5) is slightly below 2 N, consistent with our estimation since careful inspection of the results show us that velocity does not go to zero in a single step but rather it takes about two steps and therefore the impulsive response has a wider support and smaller magnitude.
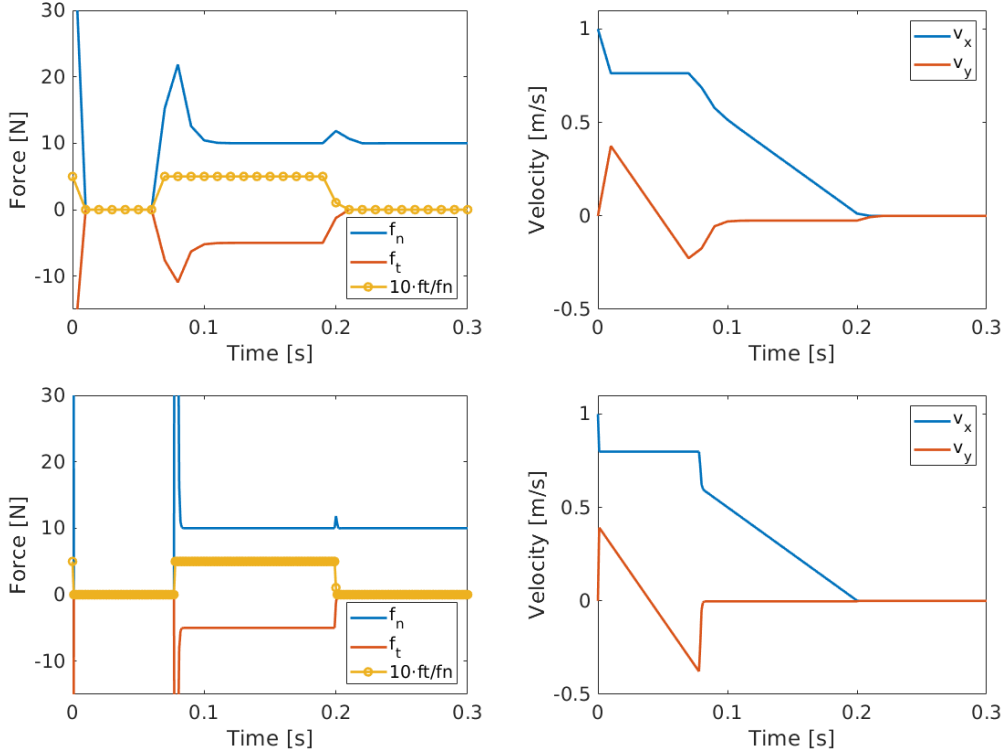

Figure 4: Horizontal u and vertical v velocities (left) and contact forces (right) as a function of time. Oscillations during sliding are a consequence of the convex relaxation which introduces a dependence of the normal forces on the sliding velocity.

6.3 Clutter

The purpose of this case is to evaluate the scalability of this method with problem size. The setup consists of an open container of 80 cm × 80 cm and 40 cm of height. Objects are dropped into this container from four different piles of ten objects each, as shown in the upper left corner of Fig. 6. Each pile consists of an arbitrary assortment of spheres of radii 5 cm and boxes with sides 10 cm in length. To emulate multi-contact, boxes are augmented with an array of 3×3 points on each face, shown as red spheres in Fig. 6.

Figure 6 shows snapshots of the solution computed with $dt = 10^{-2}$ s. The number of contacts increases over time as the objects settle in a clutter within the container, as shown in Fig. 7. Notice these are the number of contact constraints per time step. The number of active contacts will be smaller.

Figure 8 shows the simulation time step dt divided by the wall-clock time per step, an estimate of the real-time factor. These are very early performance results only evaluated using Gurobi. Other solutions strategies might perform better. We make a number of observations:
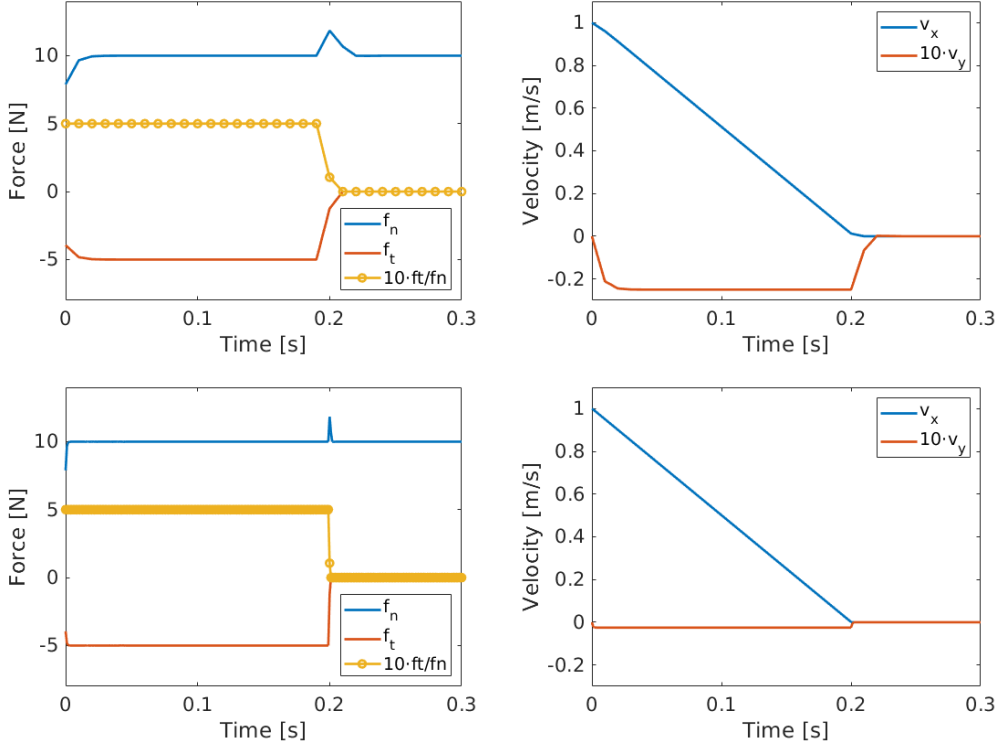
Figure 5: Horizontal u and vertical v velocities (left) and contact forces (right) as a function of time. Oscillations during sliding are a consequence of the convex relaxation which introduces a dependence of the normal forces on the sliding velocity.

1. As expected, the real-time factor increases as we use a larger time step, of course at the expense of a lower accuracy.

2. There is a region below about 20 contacts, where the solver performs faster than real-time.

3. Beyond 20 contacts and up to about 150 contacts the curves show little statistical noise.

4. Beyond 150 contacts the curves show significantly higher statistical noise. We believe this is a consequence of the inability to warm start interior point methods.

7   Future Research Directions

As shown in the clutter example in Section 6.3, the scheme is not quite competitive in terms of performance. Our current scheme in Drake, TAMSI [7], performs significantly better given it only needs a few Newton-Raphson iterations to converge per time step. However TAMSI becomes very unstable for large systems and in particular, it is not possible to run the clutter example with that scheme.

We'd therefore like to explore different solution strategies on the optimization problem stated in Eq. 4. We are particularly interested on schemes that allow warm-starting given that we can write a good guess using the analytical expressions presented in Section 4 from an initial guess on the velocities, which is available. In particular, we'll explore the Conex solver developed by Frank Permenter [8].

A   Analytical Inverse Dynamics Derivations

Since $\mathbf{R}_i \succ 0$, the problem in Eq. (5) can be thought of as minimizing the $\mathbf{R}$ norm of the difference $\boldsymbol{\gamma}_i - \boldsymbol{y}_i$ with $\boldsymbol{\gamma}_i$ subject to be within the local friction cone $\mathcal{F}_i$. This is a convex optimization
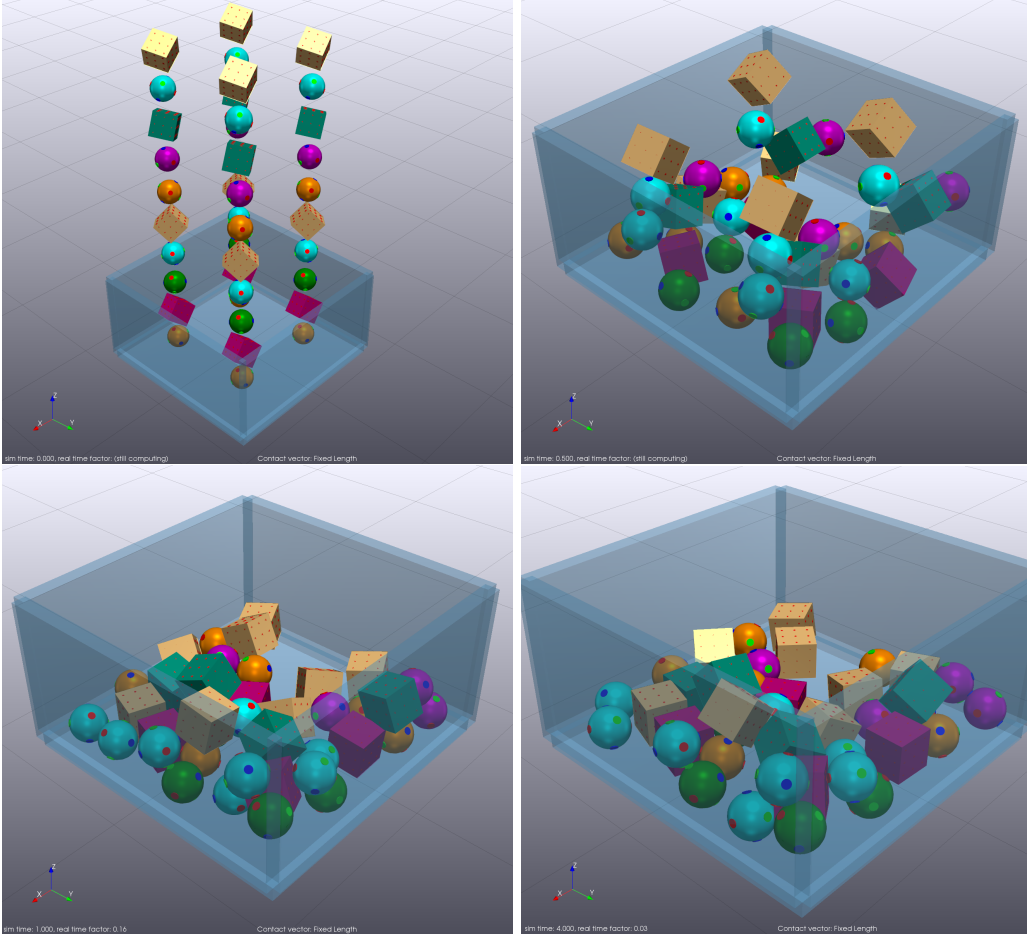
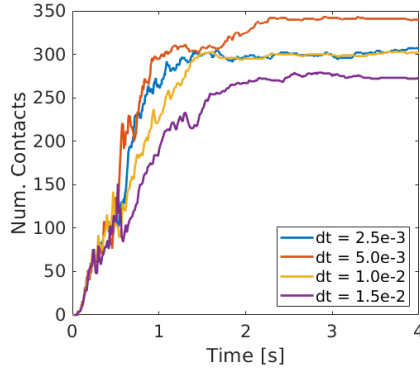Figure 6: Snapshots of the solution computed with time step $dt = 10^{-2}$ s.

Figure 7: Number of contact pairs as a function of time.

problem and can be solved analytically by simple geometry when written as a minimization in the Euclidean norm using the change of variables

$$\begin{aligned} \tilde{\boldsymbol{y}}_i &= \mathbf{R}_i^{1/2}\boldsymbol{y}_i \\ \tilde{\boldsymbol{\gamma}}_i &= \mathbf{R}_i^{1/2}\boldsymbol{\gamma}_i \end{aligned} \tag{17}$$

This leads to the equivalent problem

$$\tilde{\boldsymbol{\gamma}}_i = \underset{\tilde{\boldsymbol{x}} \in \tilde{\mathcal{F}}_i}{\arg\min} \frac{1}{2}\|\tilde{\boldsymbol{x}} - \tilde{\boldsymbol{y}}_i\|^2 \tag{18}$$
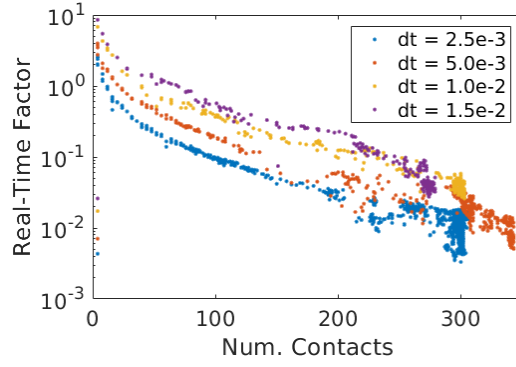
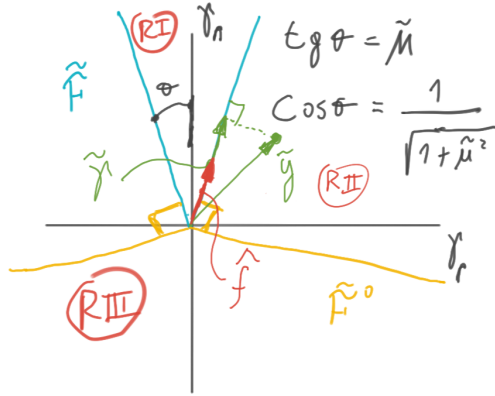Figure 8: Performance of the strategy using Gurobi's solver.

Figure 9: Geometry of $\tilde{\mathcal{F}}_i$ and regions in the $\tilde{\boldsymbol{y}}$ space.

where the friction cone *tilde* is a friction cone with an effective friction coefficient defined as

$$\tilde{\mu}_i = \mu_i \left(\frac{R_{t,i}}{R_{n,i}} \right)^{1/2} \tag{19}$$

with R_t and R_n the tangent and normal coefficients of the regularization matrix, i.e. $\mathbf{R}_i = \mathrm{diag}(R_{t,i}, R_{t,i}, R_{n,i})$.

The optimization problem in the Euclidean norm given by Eq. (18) can be solved by inspection. If $\tilde{\boldsymbol{y}}_i \in \tilde{\mathcal{F}}_i$, then we simply have $\tilde{\boldsymbol{\gamma}}_i = \tilde{\boldsymbol{y}}_i$, we call this *Region I*. If however $\tilde{\boldsymbol{y}}_i$ is inside the negative of the dual cone (a.k.a. the *polar* cone), the closest point to $\tilde{\boldsymbol{y}}_i$ within the (tilde) friction cone is zero, i.e. $\tilde{\boldsymbol{\gamma}}_i = \boldsymbol{0}$. We call this *Region III*. Finally, if $\tilde{\boldsymbol{y}}_i$ is in the region outside both $\tilde{\mathcal{F}}_i$ and its polar $\tilde{\mathcal{F}}_i^\circ$, then the closest point is it's Euclidian projection on the boundary of $\tilde{\mathcal{F}}_i$. We call this *Region II*. Figure 9 shows a schematic of $\tilde{\mathcal{F}}_i$, $\tilde{\mathcal{F}}_i^\circ$ and labels the three different regions.

To write an analytical expresion, we define the unit vector $\hat{\boldsymbol{f}}$ along the wall of the cone as

$$\hat{\boldsymbol{f}} \quad = \quad \frac{1}{\sqrt{1+\tilde{\mu}^2}} \begin{pmatrix} \tilde{\mu}\hat{\boldsymbol{t}} \\ 1 \end{pmatrix} \tag{20}$$

with $\hat{\boldsymbol{t}}$ the unit vector in the tangent direction direction defined as

$$\hat{\boldsymbol{t}} = \frac{\tilde{\boldsymbol{y}}_t}{\|\tilde{\boldsymbol{y}}_t\|_s} = -\frac{\boldsymbol{v}_t}{\|\boldsymbol{v}_t\|_s} \tag{21}$$

and we are using the *soft norm* $\|x\|_s = \sqrt{\|x\|^2 + \varepsilon^2}$ so that $\hat{\boldsymbol{t}}$ is well defined in the limit to zero tangential velocity $\boldsymbol{v}_t$. We also define its perpendicular unit vector $\hat{\boldsymbol{f}}^\perp$ as

$$\hat{\boldsymbol{f}}^\perp \quad = \quad \frac{1}{\sqrt{1+\tilde{\mu}^2}} \begin{pmatrix} \hat{\boldsymbol{t}} \\ -\tilde{\mu} \end{pmatrix} \tag{22}$$

such that $\hat{\boldsymbol{f}} \cdot \hat{\boldsymbol{f}}^\perp = 0$. We also define the projection operators given a unit vector $\hat{\boldsymbol{x}}$ as

$$\mathbf{P}(\hat{\boldsymbol{x}}) = \quad \hat{\boldsymbol{x}} \otimes \hat{\boldsymbol{x}} \tag{23}$$

$$\mathbf{P}^\perp(\hat{\boldsymbol{x}}) = \quad \mathbf{I} - \mathbf{P}(\hat{\boldsymbol{x}}) \tag{24}$$

With these definitions we can write the solution to Eq. (18) when in region II as

$$\tilde{\boldsymbol{\gamma}}_i = \mathbf{P}(\hat{\boldsymbol{f}}_i) \, \tilde{\boldsymbol{y}}_i \tag{25}$$

leading to the final expression for the impulse

$$\boldsymbol{\gamma}_i = \mathbf{G}_i(\boldsymbol{v}_{c,i} + \boldsymbol{b}_i) \tag{26}$$

with

$$\mathbf{G}_i = \begin{cases} -\mathbf{R}_i^{-1} & \text{Region I;} \quad \tilde{\boldsymbol{y}}_i \in \tilde{\mathcal{F}}_i \\ -\mathbf{R}_i^{-1/2}\mathbf{P}(\hat{\boldsymbol{f}}_i)\mathbf{R}_i^{-1/2} & \text{Region II;} \quad \tilde{\boldsymbol{y}}_i \notin \tilde{\mathcal{F}}_i \wedge \tilde{\boldsymbol{y}}_i \notin \tilde{\mathcal{F}}_i^\circ \\ \mathbf{0}_3 & \text{Region III;} \quad \tilde{\boldsymbol{y}}_i \in \tilde{\mathcal{F}}_i^\circ \end{cases} \tag{27}$$

References

[1] M. Anitescu, "Optimization-based simulation of nonsmooth rigid multibody dynamics," *Mathematical Programming*, vol. 105, no. 1, pp. 113–143, 2006.

[2] M. Anitescu and A. Tasora, "An iterative approach for cone complementarity problems for nonsmooth dynamics," *Computational Optimization and Applications*, vol. 47, no. 2, pp. 207–235, 2010.

[3] A. Tasora and M. Anitescu, "A matrix-free cone complementarity approach for solving large-scale, nonsmooth, rigid body dynamics," *Computer Methods in Applied Mechanics and Engineering*, vol. 200, no. 5-8, pp. 439–453, 2011.

[4] E. Todorov, "Convex and analytically-invertible dynamics with contacts and constraints: Theory and implementation in mujoco," in *2014 IEEE International Conference on Robotics and Automation (ICRA)*, pp. 6054–6061, IEEE, 2014.

[5] E. Todorov, "A convex, smooth and invertible contact model for trajectory optimization," in *2011 IEEE International Conference on Robotics and Automation*, pp. 1071–1076, IEEE, 2011.

[6] H. Mazhar, D. Melanz, M. Ferris, and D. Negrut, "An analysis of several methods for handling hard-sphere frictional contact in rigid multibody dynamics," tech. rep., Citeseer, 2014.

[7] A. M. Castro, A. Qu, N. Kuppuswamy, A. Alspach, and M. Sherman, "A transition-aware method for the simulation of compliant contact with regularized friction," *IEEE Robotics and Automation Letters*, vol. 5, no. 2, pp. 1859–1866, 2020.

[8] F. Permenter, "A geodesic interior-point method for linear optimization over symmetric cones," *arXiv preprint arXiv:2008.08047*, 2020.

Todo list